

# THE QUANTITY OF INTRACLUSTER LIGHT: COMPARING THEORETICAL AND OBSERVATIONAL MEASUREMENT TECHNIQUES USING SIMULATED CLUSTERS

CRAIG S. RUDICK<sup>1,2</sup>, J. CHRISTOPHER MIHOS<sup>1</sup>, AND CAMERON K. MCBRIDE<sup>3</sup>

*Draft version July 10, 2021*

## ABSTRACT

Using a suite of  $N$ -body simulations of galaxy clusters specifically tailored to studying the intracluster light (ICL) component, we measure the quantity of ICL using a number of different methods previously employed in the literature for both observational and simulation data sets. By measuring the ICL of the clusters using multiple techniques, we are able to identify systematic differences in how each detection method identifies the ICL. We find that techniques which define the ICL solely based on the current position of the cluster luminosity, such as a surface brightness or local density threshold, tend to find less ICL than methods utilizing time or velocity information, including stellar particles' density history or binding energy. The range of ICL fractions (the fraction of the clusters' total luminosity found in the ICL component) we measure at  $z = 0$  across all our clusters using any definition span the range from 9–36%, and even within a single cluster different methods can change the measured ICL fraction by up to a factor of two. Separating the cluster's central galaxy from the surrounding ICL component is a challenge for all ICL techniques, and because the ICL is centrally concentrated within the cluster, the differences in the measured ICL quantity between techniques are largely a consequence of this central galaxy/ICL separation. We thoroughly explore the free parameters involved with each measurement method, and find that adjusting these parameters can change the measured ICL fraction by up to a factor of two. The choice of ICL definition does not strongly affect the ICL's ability to trace the major features of the cluster's dynamical evolution. While for all definitions the quantity of ICL tends to increase with time, the ICL fraction does not grow at a uniform rate, nor even monotonically under some definitions. Thus, the ICL can be used as a rough indicator of dynamical age, where more dynamically advanced clusters will on average have higher ICL fractions.

*Subject headings:* galaxies: clusters: general — galaxies: evolution — galaxies : interactions — galaxies: kinematics and dynamics — methods: numerical

## 1. INTRODUCTION

Massive galaxy clusters are known to contain a luminous component consisting of stars which reside *outside* the clusters' galaxies, often referred to as intracluster light or ICL. While ICL was first detected in deep photographic imaging (Zwicky 1951; Oemler 1973; Gudehus 1989), it is only with the advent of modern CCD imaging techniques that quantitative studies of the ICL have become possible (e.g., Uson et al. 1991; Vilchez-Gomez et al. 1994; Feldmeier et al. 2004; Mihos et al. 2005; Zibetti et al. 2005; Krick & Bernstein 2007; to name only a few). For over a decade now, increasingly precise measurements of the ICL in galaxy clusters have shown that the ICL is an important component of the cluster's overall luminosity.

Although the details of the methods through which the ICL is generated are still debated — and in fact there are likely a number of processes which contribute — the strong tidal fields generated by galactic interactions during the dynamical evolution of the cluster (Gnedin 2003) are likely to be a primary contributor (e.g., Willman et al. 2004; Rudick et al. 2006, hereafter R06; Murante et al. 2007; Conroy et al. 2007; Purcell et al. 2007; Baria et al. 2009; Yang et al. 2009; Wu & Jiang 2009; Rudick et al. 2009, hereafter R09). Thus, the ICL

is composed of material that has been stripped into the intra-cluster environment from the cluster galaxies, and is a unique product of galaxy evolution within high density environments, such as galaxy clusters. As such, it can provide a wealth of information on the dynamical history of both the cluster itself, and its constituent galaxies.

As the study of ICL has matured, it has become increasingly apparent that the precise nature and identity of the ICL is poorly defined. Numerous techniques have been developed for defining and measuring the ICL in galaxy clusters. The commonality between all ICL detection methods is that in all cases the ICL has very low surface brightness and extends well beyond the traditional outer radii of the cluster galaxies. However, each ICL classification method makes different assumptions about the distribution of luminosity in the cluster galaxies, and thus systematic differences exist between them on the precise identity, spatial distribution, and quantity of ICL. For instance, several authors have measured the ICL using an isophotal limit, whereby ICL is classified as luminosity below a given surface brightness (e.g., Feldmeier et al. 2004, Zibetti et al. 2005), while others have attempted to model and subtract the galactic light and defining the ICL as any excess luminosity (e.g., Gonzalez et al. 2005, Seigar et al. 2007). Because the study of ICL requires very deep, time consuming observations (e.g., Mihos et al. 2005; Krick et al. 2006), no single unified observational program exists containing the large number of clusters necessary for fully understanding how the ICL varies between different galaxy clusters. The lack of common, well-defined measurement techniques has hampered the ability to directly compare multiple observa-

craig.rudick@phys.ethz.ch

<sup>1</sup> Department of Astronomy, Case Western Reserve University, 10900 Euclid Ave, Cleveland, OH 44106

<sup>2</sup> Institute for Astronomy, ETH Zürich, Wolfgang-Pauli-Strasse 27, 8093 Zürich, Switzerland

<sup>3</sup> Department of Physics & Astronomy, Vanderbilt University, 6301 Stevenson Center, Nashville, TN 37235

tional studies.

Much of our understanding of the formation and evolution of the galaxy clusters' ICL component comes from cosmological simulations of cluster formation which focus on the ICL's dynamics. Once again, however, many of these studies have employed substantially different techniques for identifying and measuring the ICL component, making direct comparisons difficult. The most common method is to use a binding energy definition, whereby ICL is luminous matter which is not bound to any individual cluster galaxy. However, many different studies have used significantly different variations on this basic technique (e.g., Murante et al. 2004; Sommer-Larsen et al. 2005; Purcell et al. 2007; Dolag et al. 2010; Puchwein et al. 2010). Furthermore, such binding energy definitions differ fundamentally from observationally tractable measurements of the ICL (e.g., R06). Thus, there are not only potential systematic differences in ICL classification between studies within the observational and simulation sub-fields, but potentially larger systematic discrepancies likely exist between the observational and simulation-based approaches.

With the wide variety of ICL definitions which have been used in various studies, none can claim to be the single definitive standard. For any study of the ICL properties, the precise definition used must be carefully selected to match the particular science application. For instance, while measuring the binding energy of luminous mass to its host galaxy may not be feasible observationally, it may be an appropriate tool for studying the mechanics of gravitational stripping in the cluster environment, with the caveat that ICL fractions measured in this way will not be directly comparable to observations. Additionally, factors such as computational efficiency, repeatability, and parameter dependence must also be considered in the choice of ICL definition.

A more thorough understanding of the total quantity of ICL present in clusters thus requires studying how the most common measurement techniques function and the systematic discrepancies between the luminosity classified as ICL in each. In this paper we attempt to study and clarify the relationships between many of the most commonly used ICL classifications. We have developed a suite of simulated galaxy clusters specifically designed to study the dynamics of the ICL and galactic outskirts (first described in R06 and R09). For each of these clusters, we measure the ICL component using a number of common techniques, including some which are predominantly used on observational data sets. Section 2 describes our simulation methods and the basic properties of each of our clusters. In Section 3 we give a detailed description of each ICL measurement technique we employ. Section 4 examines the systematic differences between the morphological features identified as ICL by each of our methods. Section 5 contains a discussion of our results, particularly within the context of previous studies. Finally, Section 6 presents a summary of our main conclusions.

## 2. SIMULATED CLUSTERS

### 2.1. *Simulation Techniques*

Our method for simulating galaxy clusters was first presented in R06, and again outlined in R09. Here, we provide a brief overview of the process. Over the intervening time period, however, we have made a number of updates to the simulation techniques. The result of this methodological evolution is that we have two distinct sets of simulations, which

follow the same basic process, but certain aspects of their initialization and evolution have been altered. All simulations begin with a large (comoving box sizes of 50-150 Mpc), relatively low resolution cosmological dark matter only simulation (particle mass of  $\approx 5 \times 10^8 M_\odot$ ) run from  $z = 50$  to  $z = 0$ . Individual clusters, ranging in mass from  $8 \times 10^{13}$  to  $6 \times 10^{14} M_\odot$  (see Table 1) were selected from these cosmological simulations at  $z = 0$  to re-simulate at higher resolution, including models of the luminous galaxies within the clusters. To do this, we trace the mass which constitutes the  $z = 0$  cluster dark matter halo back to its position at  $z = 2$ . Of course, at  $z = 2$  the cluster halo has not yet formed, and the mass is instead contained in a number of individual galaxy and group-mass halos. We insert our luminous galaxy models into these halos by excising the most bound 70% of the halos' mass and replacing it with a galaxy model of the same mass. For larger, group-mass halos, we employ a halo occupation distribution, or HOD, method (Berlind & Weinberg 2002) which allows us to maintain our galaxy mass function by inserting multiple galaxies into the same halo. We use two galaxy models, based on those described in Hernquist (1993): a disk galaxy with a stellar component consisting of an exponential disk plus central bulge (with a bulge-to-disk ratio of 1:5), and an elliptical galaxy with the stars in a pure Hernquist (Hernquist 1990) distribution; additionally, both galaxy models are embedded in an isothermal dark matter halo. The mass resolution of the galaxy models is fixed, such that the luminous particles have mass  $1.4 \times 10^6 M_\odot$  with smoothing scale 280 pc, while the galactic dark matter particles have mass  $1.6 \times 10^7 M_\odot$  with smoothing scale 1.4 kpc, and the mass of a galaxy is scaled by the number of particles which resolve it. The final galaxies are thus composed of particles of three distinct mass resolutions (luminous particles, galaxy dark matter, and original cluster dark matter), with a total dark to luminous matter ratio of 10:1. The composite halos of the galaxies display an NFW-like structure (Navarro et al. 1996), declining as  $r^{-3}$  at large radii. In addition to adding the high resolution galaxy models to the cluster itself, the surrounding cosmology is down-sampled to lower resolution by randomly selecting a subset of the massive particles, and increasing their mass to maintain the cosmological mass density. The entire cosmological volume, consisting of a high resolution galaxy cluster embedded within a low resolution cosmology is then re-simulated for each cluster.

This collisionless, multi-resolution simulation technique allows us to effectively focus our computational resources on the detailed gravitational dynamics of the cluster galaxies which give rise to the ICL. The trade-off, of course, is that we neglect certain aspects of galaxy and cluster evolution which may play a role in determining the spatial distribution of luminous material in the cluster. By omitting hydrodynamic evolution, we cannot measure such processes as gas accretion, star formation, ram pressure stripping, etc. which affect the evolution of galaxies in clusters. However, such calculations are computationally expensive and contain significant uncertainties. By focusing on gravitational mechanics alone, we are able to isolate this important mechanism and study the gravitationally driven evolution of the cluster at higher resolution and in greater detail. Additionally, we have a minimum stellar mass for inserted galaxies of  $5.6 \times 10^9 M_\odot$ , or about 10% of the mass of the Milky Way. We do not have the resolution to properly simulate smaller galaxies, and thus we are unable to measure their contribution the cluster's ICL content.

TABLE 1  
BASIC PROPERTIES OF SIMULATED CLUSTERS

Cluster	$M_{200}$ [ $10^{14} M_{\odot}$ ]	$R_{200}$ [Mpc]	Simulation Methods code	Simulation Methods	
				$\alpha$	$\Omega_{\Lambda}$
C1	0.88	0.93	GADGET	-1.0	0.70
C2	0.84	0.92	GADGET	-1.0	0.70
C3	0.87	0.96	GADGET	-1.0	0.70
C2R	0.82	0.91	GADGET-2	-1.5	0.70
B22	2.2	1.3	GADGET-2	-1.5	0.75
B35	3.3	1.5	GADGET-2	-1.5	0.75
B65	6.5	1.8	GADGET-2	-1.5	0.75

\*  $M_{200}$  and  $R_{200}$  are the mass enclosed and radius, respectively, of a sphere with density 200 times the critical density.

By inserting our luminous galaxy models at  $z = 2$ , we may fail to place galaxies into halos which are below our mass limit at that time, but which later grow to exceed the limit. However, we have tested that reasonable changes of the insertion redshift do not have a strong influence on the resulting ICL properties (see R06). Despite these caveats, our simulations have been designed to faithfully trace the gravitational evolution of the galaxies evolving within clusters with sufficient resolution to trace the outermost, least bound luminosity which is most likely to be stripped to form the intracluster light.

## 2.2. Cluster Properties

There are three main ways in which our two sets of simulations differ from one another. First, our original simulations were run with the  $N$ -body code GADGET (Springel et al. 2001), while the updated method employs the more recent GADGET-2 (Springel 2005). Secondly, we updated the cosmological parameters to reflect recent results in this field (e.g., Hinshaw et al. 2009). The original simulations were run in a  $\Omega_{\Lambda} = 0.7$ ,  $\Omega_M = 0.3$ ,  $H_0 = 70$ ,  $\sigma_8 = 0.9$  cosmology, while the updated simulations use  $\Omega_{\Lambda} = 0.75$ ,  $\Omega_M = 0.25$ ,  $H_0 = 70$ ,  $\sigma_8 = 0.8$ . Finally, and perhaps most substantially, the HOD parameters in the initialization scheme were modified. In particular, the masses of the inserted galaxies were more heavily weighted to low-mass galaxies, by adjusting the low-mass slope of the galaxy mass function from  $\alpha \approx -1.0$  to  $\alpha \approx -1.5$ .

In this work we discuss the results of six simulated galaxy clusters. Clusters C1, C2, and C3 were first presented in R06. Each of these was run using the original simulation methods and all have masses of  $\approx 0.9 \times 10^{14} M_{\odot}$ . In order to explore how the dynamics of ICL production may depend on cluster mass, we have run three more massive clusters, which we refer to as B22 ( $2.2 \times 10^{14} M_{\odot}$ ), B35 ( $3.5 \times 10^{14} M_{\odot}$ ), and B65 ( $6.5 \times 10^{14} M_{\odot}$ ), each using the fully updated simulation methods. Additionally, in order to check the robustness of our simulation techniques, and to ensure that there are no systematic effects on the cluster dynamics caused by our evolving simulation methodology, we chose to re-initialize and re-simulate cluster C2, starting from the same initial dark matter distribution, but using the new initialization scheme and GADGET-2 to run the simulation. We refer to this simulation as C2R, and in general it behaves very similarly to the original C2, as expected. The basic properties of these clusters and the techniques used to simulate them are summarized in Table 1. For all analyses in this paper, we define the total cluster luminosity as the luminous material within  $1.5R_{200}$  of the cluster center of mass unless otherwise noted.

Figure 1 shows an image of each of our six clusters at  $z = 0$ . Each clusters, of course, has a unique dynamical history, and

this history is reflected in its  $z = 0$  structure. Cluster C2, for instance, is very centrally concentrated with a well defined massive central galaxy. Because of this cluster’s relaxed morphology, and its extensive use in previous studies (e.g., R06, R09), it is our most well-studied cluster simulation. For this reason, we often use this cluster in the analyses below as our prime example for demonstrating the magnitude of various effects, such as varying free parameters in our calculations.

Another cluster of particular interest is B35, our second most massive cluster. While cluster B65 is nearly twice as massive, it has the peculiar trait that at  $z = 0$  it has recently accreted a smaller cluster, and the two central galaxies are still in the process of merging (the two galaxies are difficult to distinguish in Figure 1, but are nonetheless dynamically distinct). Therefore, in several of the analyses below we also single out B35 for more intensive scrutiny, as it is our most massive cluster which has a well-defined central galaxy.

Structural analyses of the cluster galaxies have shown that the simulations suffer somewhat in quality in the inner few kpc of massive galaxies, which do not hold structural integrity over the long simulation timescale. In the first generation of simulations (run with GADGET), this problem manifested as material in the central regions of galaxies artificially losing angular momentum and settling into an overly cold central core. Because tidally stripped material comes preferentially from the outer regions of galaxies, this defect should not impact our ICL metrics in a significant way. In the second generation of simulations (run with GADGET-2), this problem was fixed, but the inner regions still suffer from continued numerical heating that lead them to become overly diffuse. While this has the potential to make our galaxies more susceptible to tidal stripping, we find no evidence of these clusters being biased toward higher ICL fractions. Again, the propensity for ICL to be stripped from the outer regions of galaxies makes the detailed dynamics of galaxy cores a less salient issue.

## 3. ICL MEASUREMENTS

There is currently no single accepted measurement technique which uniquely defines the ICL component of galaxy clusters. In this paper, we make quantitative measurements of the ICL in our simulated clusters using several techniques, similar to those that have previously been used in the literature. Our aim is thus to better understand the relationships between these techniques, in order to be able to compare the results presented in studies using varied methodologies. Moreover, any algorithm used to calculate the ICL content in clusters will involve defining free parameters, and we therefore must also understand how these free parameters affect the ICL measurements. By implementing each method on each of our clusters, we can directly compare not only the ICL content of different clusters, but we can study how the ICL content of an individual cluster changes when using different techniques.

In particular, theoretical studies based on numerical simulations and observational studies often utilize widely different ICL measurement methods, due to the very different information accessible in each. In order to help bridge this gap, we have implemented three main ICL measurement techniques. Two of these rely on three-dimensional data which are not observationally tractable, and thus are only measurable in simulation data. The third technique, however, is based on “mock imaging” of our simulated clusters, and is designed to be comparable to observational measures used on clusters in the local universe. In the sections below, we describe each measurement technique, and systematically explore the free pa-

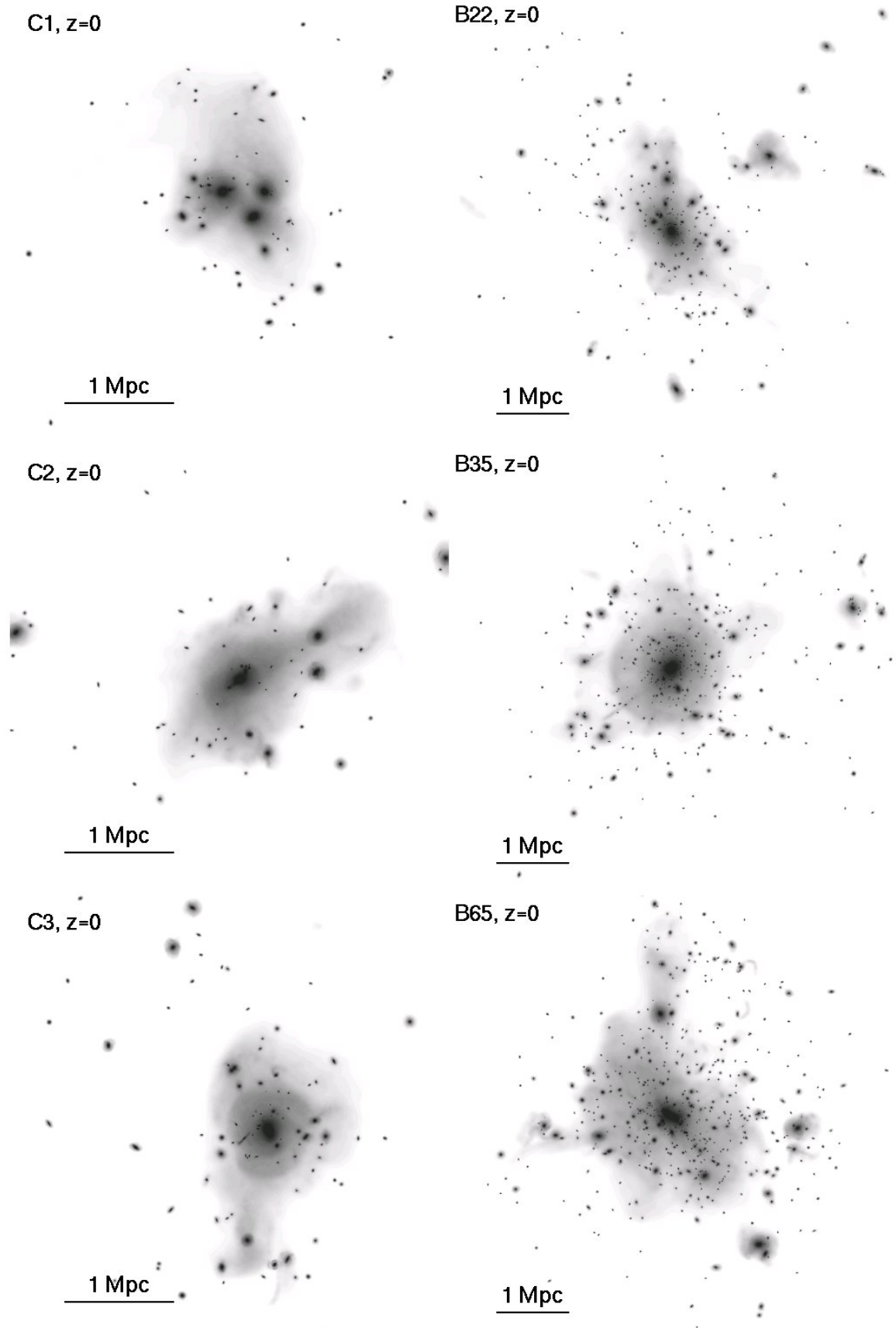


FIG. 1.— Images of the luminous component of our six clusters at  $z=0$ .

rameters on which each depends, allowing us to examine the results of each technique on our six simulated clusters. The primary metric through which we quantify the ICL content of the simulated clusters, no matter which ICL detection method we employ, is the fraction of the cluster’s luminosity that is found in the ICL component, referred to as the ICL fraction.

### 3.1. Binding Energy

One of the most appealing and commonly used definitions of ICL is that it is composed of stars which are gravitationally bound to the cluster potential, but not to any individual galaxy within the cluster. To become unbound, these stars must have been acted upon by some external force. The intense tidal fields experienced by galaxies during their evolution in a massive cluster potential provide this force, making the ICL a unique product of galactic evolution within such dense environments.

While using the binding energy of stars to define the ICL is appealing from a theoretical perspective, in practice it is quite difficult to uniquely define the potentials of individual galaxies within the cluster. Essentially, this is the same problem as identifying gravitationally self-bound sub-halos within cosmological simulations. In fact, several previous studies have used cosmological halo detection algorithms such as SKID or SUBFIND (Murante et al. 2004; Willman et al. 2005; Dolag et al. 2010) to define self-bound galaxies within the cluster and calculate the binding energy of luminous particles to these galaxies. However, there is not a single accepted technique which can uniquely define these sub-halos (see Maciejewski et al. 2009 for a discussion). Moreover, our multi-resolution simulation approach adds an additional layer of complexity to this already poorly defined problem. We have therefore not implemented such a sub-halo technique, but designed an alternative gravitational binding energy algorithm.

In order to measure the binding energy of stellar particles relative to the cluster galaxies, we have developed and implemented a technique whereby for each galaxy we measure a spherical mass density distribution with a fixed truncation radius,  $r_{trunc}$ . From such a distribution, it is quite simple to calculate the gravitational potential energy as a function of radius from the galaxy:

$$\Phi(r) = -4\pi G \left( \frac{1}{r} \int_0^r \rho(r') r'^2 dr' + \int_r^{r_{trunc}} \rho(r') r' dr' \right) \quad (1)$$

(Binney & Tremaine 2008) which allows us to efficiently measure the binding energy of each stellar particle to each galaxy, and take the ICL to be those stellar particles not bound to any galaxy. We note that a significant difference between our algorithm and most cosmological sub-halo algorithms is that we do not uniquely attribute each massive simulation particle to a particular galaxy — i.e., a single massive particle may contribute to the binding energy of multiple galaxies — nor do we uniquely assign luminosity to particular galaxies, but a luminous particle may be gravitationally bound to multiple galaxies.

In the Appendix, we provide a detailed description of our binding energy algorithm. Briefly, we begin by identifying each luminous galaxy in the cluster, and measuring its spherical mass density profile. From this profile, we define the truncation radius to be the point where the galaxy’s density profile flattens out and is dominated by the local background cluster density. With this complete density profile, we then determine for each luminous particle whether it is bound or unbound to

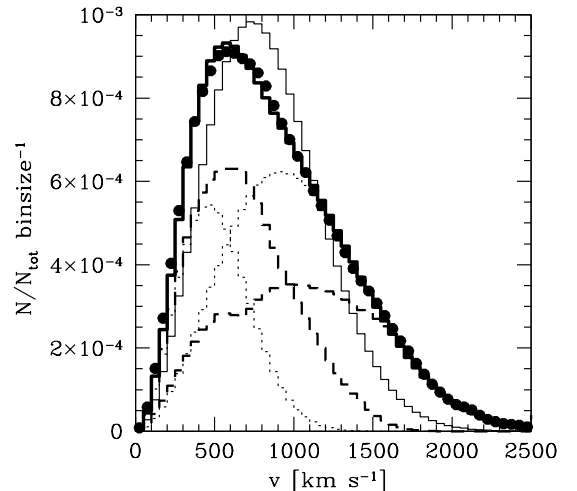


FIG. 2.— *Solid black circles*: velocity histogram of luminous particles in the inner 500 kpc of cluster B35. *Thin solid line*: best fitting Maxwellian curve to the velocity data. *Thick solid line*: best fitting double-Maxwellian curve to the velocity data. *Dotted lines*: the two components (each a single Maxwellian curve) of the best fitting double-Maxwellian, with velocity dispersions of 460 km s<sup>-1</sup> and 920 km s<sup>-1</sup>, respectively. *Dashed lines*: velocity histograms of the bound (lower velocity peak) and unbound (higher velocity peak) luminous particles in the inner 500 kpc of the cluster.

the galaxy. This procedure is repeated for all of the cluster’s galaxies, and those particles which are bound to no galaxy are identified as ICL. While this process is straightforward for the vast majority of cluster galaxies, a major challenge for the algorithm is that the mass density profile of a cluster’s central galaxy is indistinguishable from the overall cluster mass density profile. In fact, the separation of the central galaxy from the surrounding ICL component has long been a major issue confronting many binding energy-based ICL definitions (e.g., Murante et al. 2004; Sommer-Larsen et al. 2005; Dolag et al. 2010). Our particular resolution to this issue, in which we simply define a fixed truncation radius of 100 kpc for the central galaxies, is discussed in detail in the Appendix.

#### 3.1.1. Binding Energy Results

The ICL fractions which we obtain using this binding energy algorithm on our clusters at  $z = 0$  are shown in Table 2. Because of the difficulties in defining the binding energy of the many central group galaxies found at higher redshifts (a situation analogous to the clusters’ central galaxies at low redshift), we have not attempted to implement our binding energy algorithm at earlier timepoints during the clusters’ evolution. However, as a result of our galaxy initialization scheme, at  $z = 2$  every luminous particle is bound to its host galaxy.

#### 3.1.2. Kinematic Separation of the Central Galaxy and ICL

While the mass density profiles of the central galaxies do not show any features with which to distinguish them from the surrounding ICL, Dolag et al. (2010) suggest that the two populations may be separated on the basis of their kinematics. Specifically, they find that the velocity distribution of the central galaxy plus ICL component is well fit by the superposition of two Maxwellian distributions, each with a different characteristic velocity dispersion. They propose that the two Maxwellian distributions correspond to the two luminous components — the central galaxy and the ICL.

As this technique has the potential to resolve the issues described above and in the Appendix inherent in separating the

TABLE 2  
ICL FRACTIONS OF OUR SIX CLUSTERS AT  $z = 0$ , USING DEFAULT PARAMETERS FOR EACH MEASUREMENT METHOD.

Cluster	ICL Fraction			
	Binding Energy	Instantaneous Density	Density History	Surface Brightness
C1	10.5%	9.3%	14.8%	9.6%
C2	24.5%	14.6%	20.9%	13.4%
C3	19.7%	12.1%	18.5%	11.3%
B22	19.0%	9.7%	15.5%	10.2%
B35	26.3%, 36%*	11.1%	18.4%	10.4%
B65	15.8%	10.5%	15.2%	10.8%

\* using the kinematic separation of ICL from the central galaxy

central galaxy from the ICL, we have implemented a similar analysis on our simulated clusters. We use cluster B35 at  $z = 0$  to demonstrate our results, since this cluster is our most massive cluster which has a well defined central galaxy at  $z = 0$ , and is thus likely to show the clearest signatures of a distinction between central galaxy and ICL. For our lowest mass clusters, we find the Maxwellian fits to be somewhat less robust, as the velocity dispersions of the two components are more similar and thus more difficult to separate.

Figure 2 shows the velocity histogram of all particles in the inner 500 kpc of the cluster belonging to the central galaxy plus ICL components (i.e., particles not bound to any satellite galaxy). We do find that a double-Maxwellian distribution is a good fit to the velocity distribution, and the two Maxwellian components of the fit have velocity dispersions of 460 and 920  $\text{km s}^{-1}$ , respectively, in line with those expected for a cluster of this mass from Dolag et al. (2010). Integrating the two fitted Maxwellian curves, we find that the ICL component (the Maxwellian curve with the larger velocity dispersion) contains 2.3 times as much mass as the central galaxy. Given that 52.2% of the cluster’s luminosity is found in the central galaxy plus ICL components, this implies an ICL fraction for the cluster of 36%, in line with the average ICL fraction of 33% found by Dolag et al. (2010).

In addition to simply measuring the mass of the central galaxy and ICL using Maxwellian fits, Dolag et al. (2010) also separate the components on a particle-by-particle basis. They do so by adjusting the parameters of their binding energy algorithm until the velocity distributions of each of the bound and unbound components each matches one of the two components of the overall double-Maxwellian fit. We are able to achieve a similar result by reducing the truncation radius of the central galaxy to  $\approx 50$  kpc. This value, however, is small compared to the truncation radii of many of the largest satellite galaxies, which reach 100-200 kpc, and implies a central galaxy which is rather small compared to central cluster galaxies observed in the local universe (e.g., Janowiecki et al. 2010). Thus, while we are essentially able to match the results of Dolag et al. (2010), we choose not to use this method as our default means of separating the ICL from the central cluster galaxy, and continue to use our 100 kpc truncation radius as our preferred option. However, it is clear that this kinematic separation technique pioneered by Dolag et al. (2010) will result in systematically smaller central cluster galaxies, and thus a larger and more centrally concentrated ICL component, the implications of which will be discussed in the following sections.

### 3.2. Density

Another method for separating the ICL from galactic luminosity in simulation data is to define the ICL as luminous

particles with low three-dimensional density. While this definition does not measure the binding state of the particles to the galaxies, it is effective at selecting only the most isolated luminosity as ICL. We first presented our method for implementing a density-based ICL definition in R09. We reiterate the method here and apply it to all of our simulated clusters.

We calculate the density of each luminous particle as the mass density within a sphere of radius equal to the distance to the particle’s 100th nearest neighbor. Testing has shown that the density measured in this way is nearly identical to that found using the 400th nearest neighbor, as well as other density-estimation techniques.

The simplest possible density-based ICL selection criterion is to simply define a threshold density value below which particles are defined to be ICL. As in R09, our preferred value for the density threshold is  $\rho = 10^{-5.0} \text{ M}_{\odot} \text{ pc}^{-3}$ , as this limit approximately delineates a qualitative transition from smooth galaxy profiles to irregularly shaped ICL features. This effect is demonstrated in Figure 2 from R09, which shows several galaxies in our simulations and color-codes the luminous particles by their density. However, the dotted lines in the left panel of Figure 3 show the ICL fraction as function of time using several different values of the density threshold. A key feature of this figure is that while the curves show a great deal of structure, the different curves for the various ICL threshold values are essentially scaled versions of one another. That is, the major evolutionary features of the cluster which cause this structure (see Section 4) are equally well represented no matter which threshold value is used, and the different curves do not reveal unique information about the cluster’s evolutionary history. There is, however, a small but significant trend where the specific features of the cluster’s ICL evolution tend to occur at slightly later times for lower density ICL threshold levels. This result is also apparent in the surface brightness measurements found in Section 3.3, and is discussed in that Section.

The simple instantaneous density ICL detection method, however, is not able to identify ICL particles which may be located in transient high-density environments, or ICL which has migrated to near the cluster center, where the sheer number of ICL particles may in fact increase the local densities to above the threshold value (see Section 4). In order to identify such particles as ICL, we have developed a slightly more advanced density-based criterion which utilizes the density history of the luminous particles. In this method, particles which are moved to low density to become ICL *remain* classified as ICL particles, no matter their future evolution. However, in order to minimize the number of spurious ICL detections due to luminous particles on highly radial orbits around their host galaxies, we have introduced a second free parameter, a

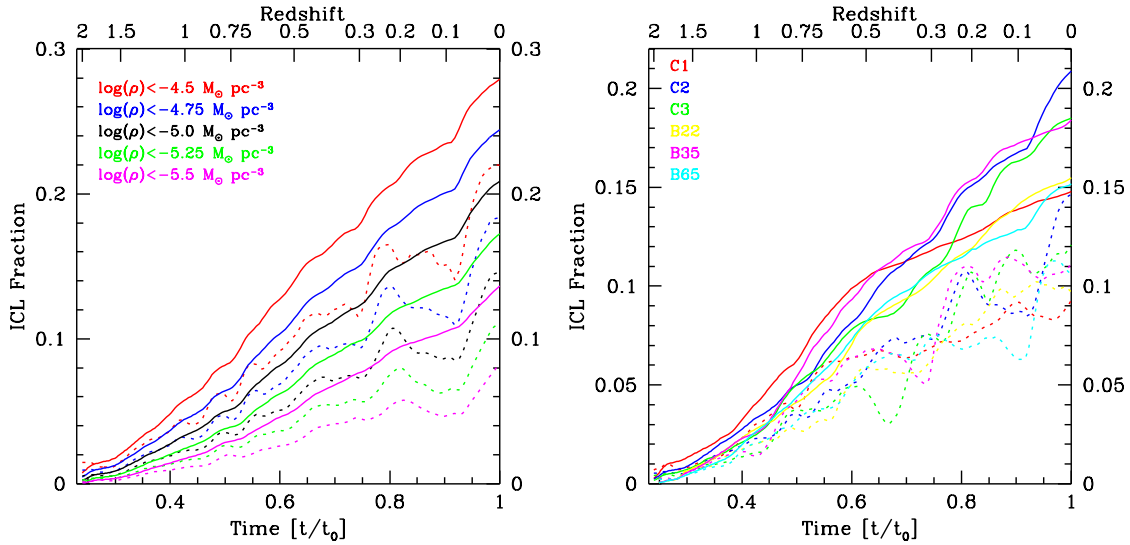


FIG. 3.— The ICL fraction measured by both the instantaneous density (dotted lines) and the density history (solid lines) methods as a function of evolutionary time. The bottom axis is in units of  $t/t_0$ , where  $t_0$  is the  $z=0$  age of the universe, while the top axis shows the corresponding redshift. *Left*: Cluster C2, using several density threshold values. *Right*: All clusters, using a threshold density value of  $\rho \leq 10^{-5.0} M_{\odot} \text{pc}^{-3}$ . Note that since the different clusters were run using slightly different cosmologies, thus marginally altering the  $t/t_0 : z$  relation, the redshifts shown correctly align with the  $t/t_0$  axis for the  $\Omega_{\Lambda} = 0.7$  cosmology, and align approximately for the  $\Omega_{\Lambda} = 0.75$  simulations.

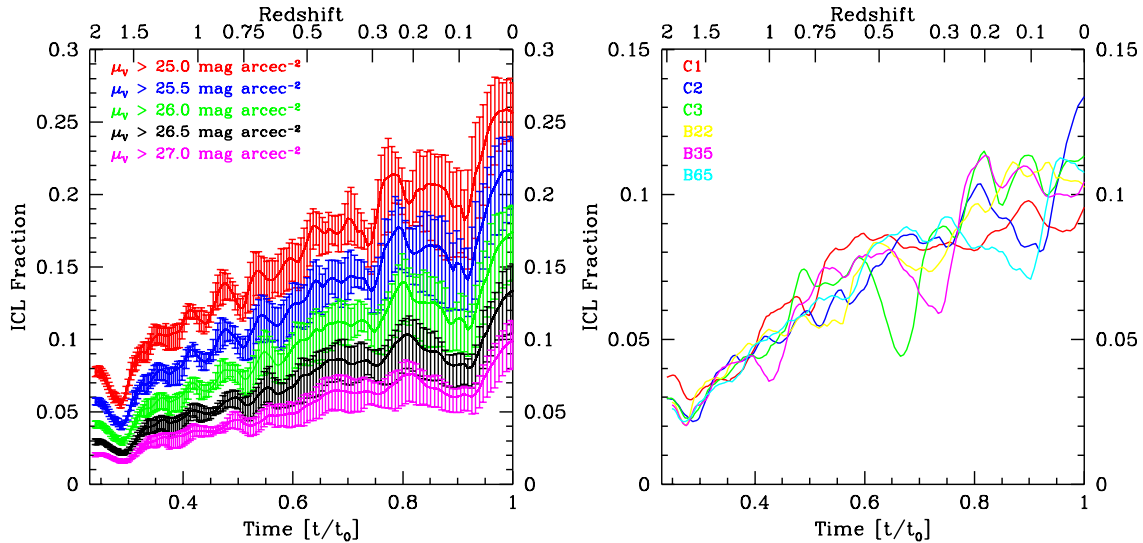


FIG. 4.— The ICL fraction measured by the surface brightness threshold definition as a function of evolutionary time. The bottom axis is in units of  $t/t_0$ , where  $t_0$  is the  $z=0$  age of the universe, while the top axis shows the corresponding redshift. *Left*: Cluster C2, using several different surface brightness threshold values. The error bars show the minimum and maximum value found for any of the nine viewing angles, and the solid line follows the mean from all viewing angles. *Right*: All clusters, using a threshold surface brightness value of  $26.5 \text{ mag arcsec}^{-2}$ . Note that since the different clusters were run using slightly different cosmologies, thus marginally altering the  $t/t_0 : z$  relation, the redshifts shown correctly align with the  $t/t_0$  axis for the  $\Omega_{\Lambda} = 0.7$  cosmology, and align approximately for the  $\Omega_{\Lambda} = 0.75$  simulations.

minimum consecutive time period for which particles must be below the threshold density value in order to be classified as ICL. The value of this minimum time period must balance the need to minimize spurious detections while also not failing to detect legitimate ICL particles which only stay at very low density for a short time, especially those which are stripped very near to the high density center of the cluster; our preferred time period value is 200 Myr. For cluster C2 increasing this time period to 500 Myr causes the ICL fraction at  $z=0$  to decrease by 3%, while removing the time minimum time period restriction causes the ICL fraction to increase by 2%.

The solid lines of Figure 3 show the ICL fraction using this density history ICL definition. A major difference between this and the instantaneous density-based ICL techniques is that with the density history it is, by definition, impossible for the ICL fraction to decrease over any time interval. Thus, for any value of the density threshold, the density history yields a higher value for the ICL fraction than the instantaneous density, except at the earliest times. For our preferred value of the density threshold,  $\rho \leq 10^{-5.0} M_{\odot} \text{pc}^{-3}$ , the difference in the ICL fraction at  $z=0$  between the two density-based methods is 6.2% of the cluster luminosity.

The ICL fraction evolution for all of our simulated clusters, using both density-based ICL detection methods, is shown in the right panel of Figure 3 and the  $z = 0$  values are recorded in Table 2, using our preferred density threshold value of  $\rho \leq 10^{-5.0} M_{\odot} \text{pc}^{-3}$ . While each cluster shows its own unique pattern of ICL production corresponding to its particular dynamical history, all the clusters show a similar trend of increasing ICL fraction with time. For most of their histories, all of the clusters’ ICL fractions lie within a fairly narrow range of a few percent. At  $z = 0$ , the smallest ICL fractions belong to C1, at 9.2% and 14.7% for the instantaneous density and density history methods, respectively, while the largest ICL fraction belong to C2, with 14.6% and 20.8% of the cluster luminosity in the ICL component under the two definitions. Thus, we see that the production of ICL by moving luminous material from high to low local densities is a common feature of clusters evolution, and that the ICL fraction is correlated to the dynamical age of the cluster, although there are variations due to the specific dynamics of each cluster.

### 3.3. Surface Brightness

In order to be able to directly compare the results of our simulated clusters to observational studies of ICL, we have generated surface brightness maps, or “mock images” of our clusters. We first introduced this imaging method in R06, in which we measured the ICL content of our clusters by setting a surface brightness threshold, and defining ICL to be luminosity at surface brightnesses fainter than the threshold. This ICL definition is, in fact, analogous to the instantaneous density definition presented in Section 3.2, in that surface brightness is essentially a measurement of the two-dimensional surface density of stellar mass, instead of the full three-dimensional volume density. In R06 our primary goal was to examine the dynamical mechanisms which generated the ICL throughout the lifetime of the cluster. Here, we focus on understanding the ICL measurement method itself — what morphological features are classified as ICL, how this compares to other ICL definitions, and how these results vary based on the exact parameters used in the algorithm.

Our method for generating surface brightness maps from our simulated clusters was first described in R06. Here we reiterate the basic procedure for convenience. We begin by projecting the luminous particle distribution onto two dimensions, binned into 1 kpc pixels. In order to create a smooth mass distribution from the discrete luminous particles, we smooth each particle using a 2-dimensional Gaussian kernel, with the smoothing scale,  $h$ , proportional to the local 3-dimensional density of each particle,  $\rho$ , by  $h \propto \rho^{-1/3}$ , similar to an SPH-type smoothing algorithm. The maximum value of the smoothing scale was set to 100 kpc for the lowest density particles, and the smoothing kernel was truncated at  $4\sigma$ .

From this smooth mass distribution, we create a luminosity, and thus surface brightness, map by applying a mass-to-light ratio to convert from stellar mass to luminosity. However, from our collisionless  $N$ -body simulation method, we have no information on the ages or metallicities of the stellar features. We have therefore chosen to apply a uniform mass-to-light ratio to all stellar particles at all redshifts. We use a mass-to-light ratio of  $5 M_{\odot} L_{\odot}^{-1}$ , a characteristic value for the  $V$ -band light of the older stellar populations we expect to find in galaxy clusters (Williams et al. 2007, Rudick et al. 2010). This unchanging mass-to-light ratio isolates the dynamical evolution of the cluster as the sole driver of the

evolving surface brightness distribution, and thus ensures that we are not conflating dynamical evolution with stellar evolution. One of the ramifications of this constant mass-to-light ratio is that the simulated images of our clusters at high redshift are not meant to match actual observations of high redshift clusters, but instead may be interpreted as images of the clusters at varying dynamical ages, but containing galaxies with similarly old stellar populations.

Given our surface brightness maps of the clusters, the simplest possible definition of ICL is to use a surface brightness cutoff to distinguish high-surface brightness galactic light from low-surface brightness ICL. In R06 we chose  $\mu_V = 26.5 \text{ mag arcsec}^{-2}$  as our ICL cutoff. This surface brightness not only corresponds to the Holmberg radius (Holmberg 1958), a commonly used metric to determine the spatial extent of galaxies, but also marks a qualitative transition where the ICL begins to take on a distinct morphology from the galactic light in both these simulations, as well as in observational works (Feldmeier et al. 2004, Mihos et al. 2005, Rudick et al. 2010). In this work we more thoroughly examine the effect of this surface brightness limit on the measured quantity of ICL. The left panel of Figure 4 shows the ICL fraction as a function of evolutionary time for several different choices of the ICL surface brightness cutoff. One feature of this surface brightness definition, described in detail in R06, is that for none of the surface brightness thresholds does the ICL fraction approach zero, even at our simulation initialization. This effect is due to the fact that all galaxies, even those that remain completely tidally undisturbed, have some small amount of material in their outermost, low-surface brightness regions, which will be classified as ICL under this definition.

Just as was seen for the density-based ICL definitions in the left panel of Figure 3, the curves for each of the ICL surface brightness thresholds are essentially scaled versions of one another and do not reveal unique information about the cluster’s evolutionary history. However, also similarly to Figure 3, there is a small but significant trend where the specific features of the cluster’s ICL evolution tend to occur at slightly later times for fainter ICL cutoff levels. Given the fundamental similarities between these two ICL measurement techniques, it is unsurprising that this phenomenon manifests itself similarly in each. These results are in excellent agreement with the findings of R06, which showed a similar trend when examining the ICL evolution at  $\mu_V \geq 26.5$  and  $\mu_V \geq 30.0 \text{ mag arcsec}^{-2}$ . This time lag indicates that while the evolutionary dynamics which drive the ICL evolution (see Section 4) can be seen equally well using any surface brightness cutoff level or density threshold value, features at lower densities and surface brightnesses probe events which occurred in the more distant past. Thus, while at a given time the relative ICL fractions measured using different surface brightness cutoffs or density thresholds give some indication of the timing of ICL production events, all are fundamentally probing the same events.

An important difference between this surface-brightness definition of ICL versus either the binding energy or density-based ICL definitions is that the surface brightness method does not classify individual luminous particles in the simulations as ICL or not. Instead, the luminosity in each pixel is defined as ICL or galactic based on the pixel’s surface brightness. Because the luminosity in each pixel is the result of the smoothed distribution of luminous particles, each pixel contains luminosity originating from many different particles,

and a single luminous particle may contribute to the luminosity in pixels of both galactic and ICL surface brightness. This distinction does not prevent us from comparing the ICL fractions measured between this and other definitions, but it does prevent us from comparing the results of the surface brightness definition with those of the other definitions on a particle-by-particle basis (see Section 4).

Because of the nature of observational metrics which project the three-dimensional structure of the clusters onto two dimensions, the precise viewing angle at which the clusters are observed can affect the resulting ICL measurements. The effects of changing the viewing angle on the ICL fraction of cluster C2 is also shown in the left panel of Figure 4. At each timepoint, we image the cluster from nine different viewing angles, chosen so that they are approximately evenly spaced on a sphere, and measure the ICL fraction of each. The error bars show the minimum and maximum values for any of these viewing angles, and the solid line follows the mean from all viewing angles. While the major evolutionary trends are similar for all viewing angles, the absolute value of the ICL fraction varies by  $\pm \approx 2\%$  at  $z = 0$ , across the different viewing angles.

Figure 4 shows the  $\mu_V \geq 26.5$  mag arcsec<sup>-2</sup> ICL fractions, as a function of time, for all six simulated clusters, and Table 2 lists the values at  $z = 0$ . Once again, these results are very similar to those seen in Figure 3 for the density-based ICL definitions. Each cluster’s ICL fraction grows as a function of time following a unique pattern related to its dynamical history. However, all the clusters stay within a relatively small range of a few percent for most of their evolution. At  $z = 0$ , the smallest ICL fraction, again belonging to cluster C1, is 9.5% while the largest is again cluster C2 with 13.2%. Just as galaxy evolution within the cluster environment inexorably moves luminous material from high to low density, it also moves luminosity from high to low surface brightness.

#### 4. MORPHOLOGICAL FEATURES OF THE ICL

Each of the ICL definitions presented in Section 3 is designed to identify stellar material in our simulated clusters that has been stripped from the individual galaxies during their evolution within the cluster. However, because each does so in a unique manner, we expect that both the qualitative features and measured quantity of ICL to vary between the different techniques. We stress, however, that there does not exist an unambiguous definition of what is or should be classified as ICL and there is thus no single criterion with which to judge the quality of any given definition. In this section, we aim to better understand the morphological features which are defined as ICL under each of our implemented definitions, and how these ICL features relate to the clusters’ evolution and dynamics by analyzing the spatial distribution, total quantity, and time evolution of the ICL in our simulated clusters.

Much about the nature of ICL, the dynamics which produce it, and the specific characteristics of each ICL definition, can be deduced simply from its spatial distribution. Figure 5 and shows several methods which we have used to study the spatial distribution of ICL in cluster C2 at  $z = 0$ . The left panel of Figure 5 shows a map of the cluster’s luminous particles, color coded based on whether or not they are identified as ICL using several of our techniques. On the top right of Figure 5 each particle’s density is plotted against its distance from the cluster’s center of mass, again color coded by ICL status. Finally, the bottom right of Figure 5 shows the radial distribution of the ICL for each of our definitions (excluding

surface brightness, since it does not identify specific particles as ICL, as discussed in Section 3.3).

From Figures 5, a number of key features of the ICL’s spatial distribution are apparent. First, the cluster can be roughly divided into two regions: an inner core where the densities of all particles are above the density threshold used in the density-based ICL definitions, and the outer regions where the densities can drop below this limit. The core is approximately ellipsoidal in shape and centered on the cluster’s central galaxy. The main feature which distinguishes the core is, of course, that none of the particles in this region can be classified as ICL based on their instantaneous density. However, a number of particles classified as ICL based on their density history are found in this region, and are the primary reason that the density history produces a higher ICL fraction than the instantaneous density definition. These particles must have either been stripped outside the core and migrated inward, or been stripped early in the cluster’s evolution before the core formed. Newly stripped particles within the core are likely to remain in this high density region — especially when stripped from galaxies on circular orbits at small radii — and therefore will not be classified as ICL based on their density history. This is not the case, however, for ICL identified by binding energy, since this definition is not in any way dependent on the local density, and even at very small radius, the intense gravitational forces are capable of unbinding some stellar particles. This population of small-radius, and thus high-density, unbound particles is the major reason the binding energy definition produces the highest ICL fraction for this cluster. Moreover, as noted in Section 3.1.2, a kinematic separation of the central galaxy and ICL would only further increase the ICL fraction by identifying many more ICL particles at the smallest radii.

Outside of the core, the vast majority of particles tagged as ICL in one definition are also identified in the others. There are, however, two notable exceptions to this trend, both particularly apparent at the outskirts of the cluster’s largest satellite galaxies. First, a significant population of particles, especially in the inner regions of recently created tidal streams, are classified as ICL by instantaneous density and density history, although are bound to their host galaxies. This suggests that material stripped from satellite galaxies may not immediately become unbound from its host, although it is likely to become unbound during its subsequent evolution. Secondly, there is a population of particles identified as ICL by density history, although currently above the instantaneous density threshold. While some of these are simply particles on highly radial orbits, others have truly been tidally stripped and then re-accreted by the galaxy.

The majority of the discrepancies between our ICL definitions occur in the inner core of the cluster. Although the direct algorithmic cause of this phenomenon is the region’s high densities, more fundamentally it points toward the fact that there is no clear distinction between the cluster’s central galaxy and its extended ICL envelope, just as in Section 3.1 we saw that the mass density profiles of central galaxies were indistinguishable from the overall cluster profiles. While we identified small differences in how the definitions identify ICL at the outskirts of satellite galaxies, these represent only a small fraction of the cluster’s ICL for two reasons: 1) the distinction between the galaxies and ICL is more clear for satellite galaxies and 2) the bulk of the cluster’s luminosity, and especially its potential ICL component, is centrally concentrated. The density versus radius plot in the top of Figure 5

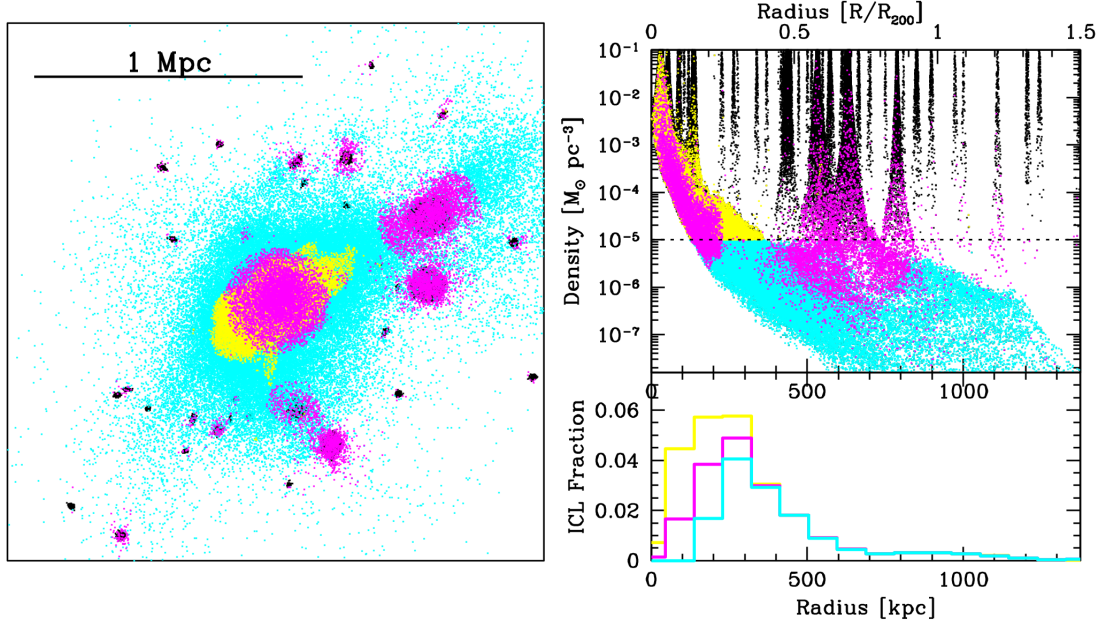


FIG. 5.— **Left:** The positions of luminous particles in cluster C2 at  $z=0$ . To increase clarity, only 3% of the particles have been plotted. Even so, in certain areas, especially the cluster center, overcrowding is a problem and particles may be over-plotted on top of one another, making certain features (such as the locations of galaxies in the cluster core) difficult to discern. *Black:* not identified as ICL using any method; *Cyan:* identified as ICL using each of the binding energy, instantaneous density, and density history methods; *Yellow:* identified as ICL from binding energy only, and not from either density-based technique; *Magenta:* identified as ICL from either or both density-based methods, but not from binding energy. Particles identified as ICL by the binding energy method but only one of the two density-based methods are very few in number, and are not shown for the sake of clarity. These classifications do not utilize our surface brightness definition since it does not classify ICL on a particle-by-particle basis; due to the similarities between instantaneous density and surface brightness, however, there is an excellent correlation between the two definitions and, in general, areas of low instantaneous density will have low surface brightness. **Right:** The radial distribution of ICL in cluster C2 at  $z=0$ . The bottom axis shows the cluster-centric radius in kpc, while the top axis shows the corresponding radius in terms of the cluster’s  $R_{200}$ . *Top:* The cluster-centric radius of each particle plotted against its density. The ICL status of the particles is delineated using the same colors as in the left panel. The dotted line shows  $\rho = 10^{-5} M_{\odot} \text{pc}^{-3}$ , the value of the density threshold. Each thin pyramidal structure at high density corresponds to an individual galaxy. Note that the cluster center ( $R=0$ ) is defined as the center of mass of the cluster, and the cluster’s massive central galaxy sits  $\approx 30$  kpc from this center. *Bottom:* Histograms of the ICL fraction (measured as the ratio of ICL in the bin to total cluster luminosity) in radial bins from the cluster center for three of our ICL definitions: binding energy (yellow, filled), instantaneous density (cyan, hatched), and density history (magenta, hatched).

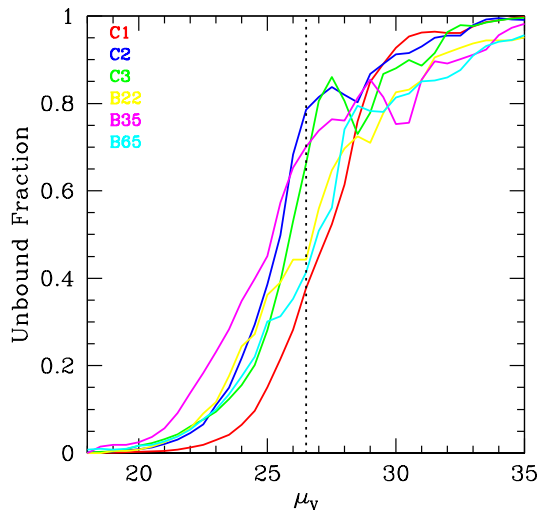


FIG. 6.— The fraction of luminosity at a given surface brightness which is contributed by unbound stars for each of our clusters.

shows a very clear locus of luminous particles extending outward from the central galaxy. This locus contains the bulk of the ICL luminosity under any definition, however there are no obvious features along the locus which can be used to separate the light of the central galaxy from the ICL. Under any of our ICL definitions, the primary effect of changing the tech-

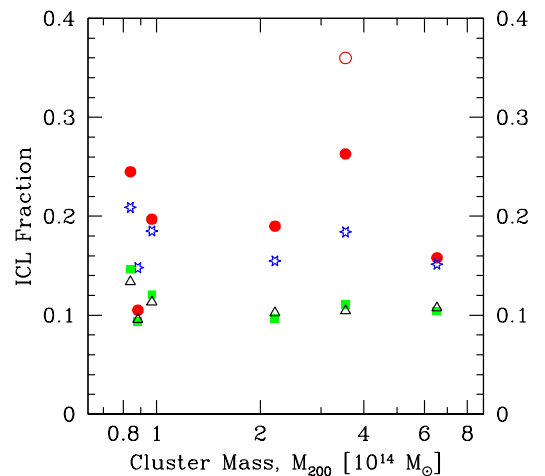


FIG. 7.— The ICL fraction of each cluster, using each of our four definitions, versus the cluster mass. Each point type corresponds to a different ICL definition: binding energy (red solid circles), binding energy using a kinematic separation of central galaxy and ICL (red open circle), instantaneous density (black open triangles), density history (blue stars), and surface brightness (green solid squares).

nique’s free parameters is to change the subset of particles along this locus that is classified as ICL. In Section 3.1, we explicitly showed that the binding energy of luminous particles to the central galaxy is poorly determined, and that the

ICL fraction using this definition is very heavily influenced by the precise parameters used to define the central galaxy. Figure 5 also makes clear that adjusting the free parameters of the density-based definitions (and, by analogy, the surface brightness definition; or see Figure 5 of R06) also primarily changes the ICL fraction by affecting the ICL surrounding the central galaxy.

One consequence of the highly centrally-concentrated nature of the ICL is that our measured ICL fractions tend to increase slightly when the outer regions of the cluster are excluded. For instance, the ICL fraction of cluster C2 measured by binding energy within  $R_{500}$  is 28.1%, a modest increase from 24.5% measured within our fiducial  $1.5 R_{200}$  limit. Of all of our ICL definitions, the binding energy method, being the most centrally concentrated, is the most affected by this change in limiting cluster radius. The ICL fraction measured by density history, for example, increases from 20.9% within  $1.5 R_{200}$ , to only 21.9% within  $R_{500}$ , and the other definitions show similarly small changes. Therefore, while the choice of limiting cluster radius may have a small systematic influence on the measured ICL quantities, the main results described in this work are not highly dependent on this choice.

While we are unable to compare our density or binding energy-based ICL definitions to our surface brightness threshold on a particle-by-particle basis, we still wish to explore the observable properties of the ICL identified with these methods. In particular, Figure 6 shows the surface brightness of the unbound stars (i.e. ICL by binding energy) by plotting the fraction of the cluster luminosity which is unbound at a given surface brightness for each of our six clusters. These measurements were made by creating “mock images” of only the unbound stellar populations of the clusters using exactly the same methodology as in Section 3.3 and comparing them to the original images. While there are subtle differences in the slopes of the curve for each cluster, they all display a distinctive S-shaped trend. At surface brightnesses brighter than  $\mu_V \approx 21$ , an extremely small fraction of light is contributed by unbound stars. At fainter surface brightnesses, however, the contribution of the unbound stars quickly increases. At surface brightnesses fainter than  $\mu_V$  of 26.5, our default surface brightness threshold for ICL, unbound stars contribute  $\gtrsim 50\%$  of the luminosity. At the very faintest surface brightnesses, of course, the unbound fractions converge toward unity, as the vast majority of the stellar material at these surface brightnesses is unbound. These results highlight the fact that while there is certainly a correlation where unbound material tends to be observed at faint surface brightness, there does exist some unbound material at relatively bright surface brightness, and vice-versa. Inspection of the images generated using only unbound stars confirm that the vast majority of the high-surface brightness unbound material is centrally concentrated in the cluster core, where the projected luminosity densities are highest. Conversely, the bound material at very low surface brightness comes primarily from tidal features around galaxies outside the core of the cluster, where material can remain loosely bound to its parent galaxy for some time before being fully stripped by the cluster potential. These results are in direct analogy to the instantaneous density definition which does not identify ICL in the innermost regions of the cluster due to the high volume-densities of luminous particles, but does immediately classify the material in tidal streams as ICL, thus re-confirming the similarities between the surface brightness and instantaneous density methods.

Given that each definition we have presented selects a dif-

ferent population of luminous particles as the ICL, it is unsurprising that the total measured quantity of ICL in the cluster is dependent on which definition is chosen. For instance, the fact that an instantaneous density definition does not identify as ICL any luminosity near the cluster core causes the ICL fraction measured using this method to be lower than those measured using either the density history or binding energy techniques. Because of the innate similarities between the instantaneous density and surface brightness, the surface brightness-based definition of ICL displays a similar effect. One interpretation of this phenomenon is that the specific morphology of a cluster may be able to “hide” stripped stellar material that is spatially coincident with the cluster’s galaxies from ICL definitions which rely on position only, such as instantaneous density and surface brightness. In fact, this geometric effect is also readily apparent in the surface brightness ICL definition, as it is the primary cause of the small variance in the ICL fraction based on the viewing angle.

To further illustrate the variance in ICL fraction that is found between different ICL definitions, Figure 7 plots the measured ICL fractions for each of our clusters at  $z = 0$ , using all four of our ICL definitions. These results show that the basic results discussed above in relation to cluster C2’s ICL features also hold for our other clusters. For instance, in each case the surface brightness and instantaneous density definitions not only give the lowest ICL fraction values of the four definitions, but these ICL fractions differ by a maximum of 1.2%, thus re-confirming the strong similarities between these definitions. The ICL fractions from density history and binding energy, however, are significantly higher, and in all but one case are higher than the ICL fraction from instantaneous density by at least 5%. The one exception is the binding energy ICL fraction calculated for cluster C1; this cluster displays a unique morphology with three nearly equal-mass large galaxies near the cluster center. Such a scenario exacerbates the difficulties in dealing with central galaxies that are inherent in binding energy definitions, and the fact that an unusually large fraction of the cluster’s luminosity is bound to these galaxies only further demonstrates that massive central galaxies play a unique role in determining a cluster’s ICL content. Additionally, from the results of Section 3.1.2 we can infer that using a kinematic separation of the ICL from the central galaxy would be likely to generate the highest ICL fractions for nearly every cluster (the results of such a separation on cluster C1, however, without a single central galaxy, remain poorly constrained).

Figure 7 not only plots the measured ICL fractions for each of our clusters, but does so as a function of the cluster mass. We do not find any trend of increasing or decreasing ICL fraction with cluster mass using any of our ICL definitions. While some studies have reported a trend where higher mass clusters tend to have greater ICL fractions (Murante et al. 2007; Purcell et al. 2007), other works have seen little evidence for such a trend (Dolag et al. 2010; Puchwein et al. 2010). Given our very limited sample size and the wide scatter found in those studies which find a trend with mass, we do not feel that our results are able to support or refute either scenario.

While the properties of the ICL in our clusters at  $z = 0$  provide insight into the morphological features identified as ICL using our various definitions, an even greater understanding of the dynamical evolution of the clusters can be gained from the evolution of the ICL fraction as a function of time. Figure 8 shows the ICL fraction as a function of time for both cluster C2 and B35, using each of our definitions; the binding energy

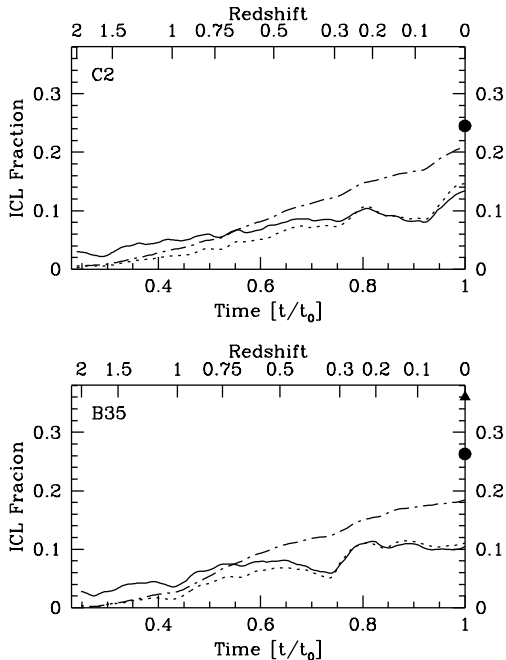


FIG. 8.— The ICL fraction as a function of evolutionary time, using each of our four ICL definitions, for clusters C2 (top) and B35 (bottom). Each line type corresponds to a different ICL definition: instantaneous density (dotted line), density history (dash-dot line), and surface brightness (solid line). The binding energy ICL fraction is only calculated at  $z = 0$ , and is shown with a closed circle and the binding energy variant using a kinematic separation of the ICL is shown at  $z = 0$  for cluster B35 as a solid triangle; the ICL fraction using the binding energy definition at  $z = 2$  is precisely zero for both clusters. The bottom axis is in units of  $t/t_0$ , where  $t_0$  is the  $z = 0$  age of the universe, while the top axis shows the corresponding redshift.

ICL fraction is shown only at  $z = 0$  since it is not calculated at every timepoint for the reasons discussed in Section 3.1, and is exactly zero at the cluster’s initialization at  $z = 2$ . As expected, no matter the definition, each of the clusters shows an increasing ICL fraction as a function of time as a result of tidal stripping within the galaxy cluster. Importantly, however, the ICL fraction does not increase at a constant rate under any ICL definition for which we have time series data, and under the surface brightness and instantaneous density definitions the increase is not entirely monotonic. This is a result that was previously discussed in both R06 and R09, where major ICL production events were found to be correlated with specific galactic interactions occurring within the cluster. In Figure 8 we see that these ICL production events occur at essentially the same times, and are of similar magnitudes, under each the different ICL definitions. This implies that each definition is primarily affected by the same events, and that any of these definitions are effective at tracing the dynamical history of the cluster.

The same variability in the cluster’s evolving ICL fraction that provides information on its dynamical history, also implies that at any single timepoint the ICL fraction alone is not a robust indicator of the cluster’s dynamical state. For instance, over the last gigayear of cluster C2’s evolution, the ICL fraction based on the surface brightness definition increases by 4.3% of the cluster’s luminosity, which is over 30% of the total  $z = 0$  ICL fraction of 13.4%. Thus, while we can expect that, on average, a cluster’s ICL fraction will increase as it dynamically ages, there is not a direct 1:1 correlation between the two. When comparing clusters, we can expect that,

on average, clusters with higher ICL fractions will be more dynamically advanced than clusters with lower ICL fractions. Although the short-term variations of the ICL fraction make such comparisons unreliable for individual clusters, it may be a metric well-suited to studying large populations of clusters statistically, such as that of Zibetti et al. (2005) using clusters from SDSS. Similarly, several theoretical studies have measured the mean and variance of the ICL fraction as a function of cluster mass using large samples of simulated clusters (Murrante et al. 2004; Purcell et al. 2007, Dolag et al. 2010).

Even if the precise ICL fraction of a cluster may have a somewhat ambiguous relationship to its dynamics, it is clear that the evolution of galaxies within the cluster environment invariably generates a significant ICL component. Using any of our ICL definition, the  $z = 0$  ICL fractions for our clusters range from 9–36%. Obviously, the ranges within a single definition, for a single set of parameters, are much smaller, but this wide range illustrates that point that no matter how the ICL is defined a significant population is present. Although this range is not meant to put definitive limits on the range of possible ICL values in observed clusters using any ICL definition, it demonstrates that all massive clusters at low redshift are expected to have at least some observable ICL component, but that the majority of the clusters’ stars should still be contained within the galaxies themselves.

## 5. DISCUSSION

Comparing the ICL fractions measured for our simulated clusters to those found in the literature using similar techniques, we generally find excellent agreement. For instance, Feldmeier et al. (2004) use a pure isophotal limit to measure the ICL in a number of observed clusters, and find ICL fractions of 7–15% when using  $\mu_V \geq 26.5$ , in excellent agreement with the 9–13% range we measure in our simulations. Simulation-based measurements which use a binding energy definition of ICL, however, tend to find somewhat higher ICL fractions. Several examples of such studies, each using unique variation of the binding energy method, include: Murrante et al. (2007) who measure ICL fractions of  $\approx 10–30\%$ ; Sommer-Larsen et al. (2005) who find  $\approx 20–40\%$  of the cluster luminosity in the ICL; and Purcell et al. (2007) who report ICL fractions ranging from  $\approx 20–30\%$  for massive clusters. Again, these match closely to the 10–26% ICL fraction range that we find using our binding energy technique, and fit with our expectation that a binding energy definition produces a higher ICL fraction than an isophotal limit. Additionally, the variant of the binding energy technique which uses kinematics to separate the central galaxy from the surrounding ICL, produces potentially the highest ICL fractions, with a range of  $\approx 20–50\%$  and mean of 33% given in Dolag et al. (2010), which matches the 36% measured for or cluster B35.

In addition to a simple surface brightness threshold, there is a second commonly used definition of ICL measured from deep surface photometric observations. In this method, the cluster’s galactic light is modeled with idealized galaxy profiles and subtracted, with the residual light defined as the ICL (e.g., Gonzalez et al. 2005; Seigar et al. 2007). In particular, this method is commonly used on cD galaxies, which traditionally have been defined as central galaxies which display a “double de Vaucouleurs” profile, or an excess of luminosity at large radius over the traditional de Vaucouleurs profile, which is then fit by a second de Vaucouleurs profile (e.g., de Vaucouleurs 1953; Matthews et al. 1964; Oemler 1973; Feldmeier et al. 2002; Gonzalez et al. 2005). The integrated light of

this second, outer profile is taken to be the ICL. This method potentially resolves the discrepancy between the theoretically favored binding energy definition of ICL and our observationally tractable surface brightness threshold method, whereby a surface brightness threshold does not identify stripped material at the cluster's center as ICL, since the fitted outer profile does indeed extend to the center of the galaxy. As expected, such analyses tend to yield higher ICL fractions than an isophotal cut and similar to those from simulations employing a binding energy ICL definition, with the ICL fraction typically at or above 20–30% (Seigar et al. 2007; Gonzalez et al. 2007; Zibetti et al. 2008).

While it is commonly assumed that the outer envelope is the product of tidal stripping within the cluster environment in accordance with its classification as ICL, it is unclear how well this profile truly matches with the cluster's stripped material, especially in the innermost regions which coincide with the inner, bright regions of the cD itself. Moreover, recent evidence suggests that the structure of giant elliptical galaxies in massive clusters may not be as well-defined as previously assumed (e.g., Kormendy et al. 2009). It has been suggested that cD galaxies, with their extended ICL component, may be best described as double de Vaucouleurs (e.g., Gonzalez et al. 2005), de Vaucouleurs plus an outer exponential (e.g., Seigar et al. 2007), or even a single Sérsic profile (e.g., Kormendy et al. 2009, Janowiecki et al. 2010). Given the uncertainty of the true structure of cD galaxies in clusters, it is extraordinarily difficult to accurately subtract the galactic light using these parametric methods in order to measure the ICL component in a robust and precise manner. Additionally, fitting such galactic profiles is sensitive to a large dynamic range in radii, including the galaxies' innermost regions. Given our known issues with properly resolving the structure of galactic cores, we have not been able to study such galaxy fitting measurements in our simulated clusters along side our other ICL measurement techniques. Further progress in this area will likely involve a more detailed understanding of the structure and formation of elliptical galaxies, especially within the dense cluster environment.

While the many varying definitions of ICL that have been employed to date have been an impediment to a full census of the ICL in galaxy clusters, the situation may be much improved in the future as our understanding of each ICL detection method progresses. In particular, simple definitions with few free parameters, such as an isophotal limit for observational data sets, are straightforward to implement and may prove to be more robust and repeatable measurements, which better allow direct comparisons between multiple studies than more complex galaxy profile fitting methods. For simulations of the ICL component, we detailed in Section 3.1 many of the issues inherent in a binding energy definition of ICL with which any algorithm must contend, either explicitly or implicitly. A density-based definition of ICL may lack the physically-motivated elegance of a binding energy definition, but has the advantages that it is simple to calculate and has a well-defined dependence on its free parameters, making comparisons between multiple studies easier and more robust. Moreover, in order to be directly comparable to observational data sets, simulation studies must choose metrics relying on only observationally available data, such as the the surface brightness threshold method detailed in Section 3.3.

Although the ICL component contains a significant fraction of a cluster's luminosity, simply parameterizing this content with a single number, the ICL fraction, does not fully capture

its utility or intricacy. The generation of ICL is dependent on the specific dynamics of the cluster in a very complex manner, and the difficulty in uniquely defining the ICL component only compounds this complexity. For detailed observations of individual clusters the ICL's spatial structure, kinematics, and stellar populations, along with its quantity, can provide a more complete picture of the ICL component and may be used to better relate the ICL to the cluster's dynamics. In particular, a number of observational studies have linked discrete tidal streams of ICL to specific galactic interactions within the cluster (e.g., Trentham & Mobasher 1998; Gregg & West 1998; Adami et al. 2005; Mihos et al. 2005; Rudick et al. 2010; Janowiecki et al. 2010). These streams not only allow us to probe the specific histories of the galaxies involved in the interactions, but R09 found that while most ICL is initially formed in such streams, there is an inverse correlation between the quantity of ICL in streams and the cluster's dynamical age. The stellar populations which comprise the ICL can also be used to determine its origins. For instance, most studies of the broadband colors of the ICL component have determined that its color is consistent with an old, metal-poor population similar to the outskirts of the giant elliptical galaxies found in the clusters (e.g., Zibetti et al. 2005; Pierini et al. 2008; da Rocha et al. 2008; Rudick et al. 2010). Furthermore, planetary nebulae found within the ICL population provide a means for studying the ICL's kinematics (e.g., Arnaboldi et al. 2004; Gerhard et al. 2007; Doherty et al. 2009). As sample sizes of these objects increase, they will provide an unprecedented opportunity to study the dynamics of the cluster environment, by providing a large number of probes with which to trace the cluster's gravitational potential (e.g., Willman et al. 2004; Sommer-Larsen et al. 2005) and to trace the orbits and dynamics of any ICL streams or substructures. A cluster's ICL fraction is thus only one of many tools available for investigating the ICL content of the cluster and using it to trace the cluster's dynamical history.

## 6. SUMMARY

In this paper we have applied a number of ICL detection techniques to a suite of simulated clusters designed expressly for the purposes of studying the intracluster component. Our ICL definitions include techniques which are commonly used on both observational and simulation data. We have examined precisely how each defines the ICL component, and studied the systematic differences between each method. Here we summarize our main conclusions:

- The various ICL measurement techniques produce systematically different ICL fractions. Measurements which rely exclusively on the position of the cluster luminosity, such as surface brightness or instantaneous density, tend to yield ICL fractions significantly less than methods which utilize time or velocity information, such as density history or binding energy. For example, the ICL fraction of cluster C2 at  $z=0$  is 13.4% as measured by surface brightness threshold and 24.5% by the binding energy definition. Additionally, each ICL definition relies on one or more adjustable free parameters. These parameters can change the measured ICL fractions by up to a factor of two, even within a single definition.
- The ICL measurements made using each of our techniques agree quite well with those found in the literature using similar methods. Thus, the varying ranges

for the ICL fraction found in different studies may be a manifestation of how each identifies the ICL in clusters which are in fact similar.

- Our measurements of the ICL fraction in our clusters at  $z = 0$  range from 9–36% using any method. While this is not intended to put firm bounds on the range of ICL fractions found in  $z = 0$  clusters, it does demonstrate that all massive galaxy clusters are expected to have a non-negligible ICL component.
- The majority of the discrepancies between the various ICL definitions are related to the separation of the central galaxy from the surrounding ICL. The ICL is centrally concentrated in the cluster, often around a single central galaxy, and there is often no unambiguous transition from the galaxy's extended outer profile to the ICL.
- The quantity of ICL tends to increase with time under all of our ICL definitions. However, the ICL fraction does not grow at a constant rate and is related to the specific dynamical evolution of the cluster. Although more dynamically advanced clusters will, on average, have higher ICL fractions, individual clusters at a single timepoint may deviate from this trend.

- The fact that a cluster's ICL fraction can be defined in so many different ways, leading to such widely different results, underscores the fact that the quantity of ICL alone does not fully describe this important luminous component. The morphology, stellar populations, and kinematics of the ICL each provide additional insight into its nature. Only by combining the information from each can the ICL's potential to reveal the cluster's dynamical history be fully exploited.

The authors would like to thank Heather L. Morrison, Paul Harding, and Daniel S. Akerib for many useful suggestions and for advice on defining the focus of this paper. We also thank the anonymous referee for several suggestions which improved this work. This work utilized the computing resources of the CWRU ITS High Performance Cluster, and we are indebted to its staff for their patience and expertise. C.S.R. appreciates support from the Jason J. Nassau Graduate Fellowship Fund. J.C.M. acknowledges research support from the NSF through grants ASTR 0607526 and ASTR 0707793. This research was supported in part by the National Science Foundation through TeraGrid resources provided by PSC under grant numbers TG-AST070001T and TG-AST070024.

#### REFERENCES

- Adami, C., et al. 2005, *A&A*, 429, 39
- Arnaboldi, M., Gerhard, O., Aguerrri, J. A. L., Freeman, K. C., Napolitano, N. R., Okamura, S., & Yasuda, N. 2004, *ApJ*, 614, L33
- Baria, P., Brito, W., & Martel, H. 2009, *Journal of Astrophysics and Astronomy*, 30, 1
- Berlind, A. A., & Weinberg, D. H. 2002, *ApJ*, 575, 587
- Binney, J., & Tremaine, S. 2008, *Galactic Dynamics: Second Edition*, by James Binney and Scott Tremaine. ISBN 978-0-691-13026-2 (HB). Published by Princeton University Press, Princeton, NJ USA, 2008.,
- Conroy, C., Wechsler, R. H., & Kravtsov, A. V. 2007, *ApJ*, 668, 826
- Da Rocha, C., Ziegler, B. L., & Mendes de Oliveira, C. 2008, *MNRAS*, 388, 1433
- de Vaucouleurs, G. 1953, *MNRAS*, 113, 134
- Doherty, M., et al. 2009, *A&A*, 502, 771
- Dolag, K., Murante, G., & Borgani, S. 2010, *MNRAS*, 405, 1544
- Feldmeier, J. J., Mihos, J. C., Morrison, H. L., Harding, P., Kaib, N., & Dubinski, J. 2004, *ApJ*, 609, 617
- Feldmeier, J. J., Mihos, J. C., Morrison, H. L., Rodney, S. A., & Harding, P. 2002, *ApJ*, 575, 779
- Gerhard, O., Arnaboldi, M., Freeman, K. C., Okamura, S., Kashikawa, N., & Yasuda, N. 2007, *A&A*, 468, 815
- Gnedin, O. Y. 2003, *ApJ*, 582, 141
- Gonzalez, A. H., Zabludoff, A. I., & Zaritsky, D. 2005, *ApJ*, 618, 195
- Gonzalez, A. H., Zaritsky, D., & Zabludoff, A. I. 2007, *ApJ*, 666, 147
- Gregg, M. D., & West, M. J. 1998, *Nature*, 396, 549
- Gudehus, D. H. 1989, *ApJ*, 340, 661
- Hernquist, L. 1993, *ApJS*, 86, 389
- Hernquist, L. 1990, *ApJ*, 356, 359
- Hinshaw, G., et al. 2009, *ApJS*, 180, 225
- Holmberg, E. 1958, *Meddelanden fran Lunds Astronomiska Observatorium Serie II*, 136, 1
- Janowiecki, S., Mihos, J. C., Harding, P., Feldmeier, J. J., Rudick, C., & Morrison, H. 2010, *ApJ*, 715, 972
- Kormendy, J., Fisher, D. B., Cornell, M. E., & Bender, R. 2009, *ApJS*, 182, 216
- Krick, J. E., & Bernstein, R. A. 2007, *AJ*, 134, 466
- Krick, J. E., Bernstein, R. A., & Pimblett, K. A. 2006, *AJ*, 131, 168
- Maciejewski, M., Colombi, S., Springel, V., Alard, C., & Bouchet, F. R. 2009, *MNRAS*, 396, 1329
- Mathews, T. A., Morgan, W. W., & Schmidt, M. 1964, *ApJ*, 140, 35
- Mihos, J. C., Harding, P., Feldmeier, J., & Morrison, H. 2005, *ApJ*, 631, L41
- Murante, G., et al. 2004, *ApJ*, 607, L83
- Murante, G., Giovalli, M., Gerhard, O., Arnaboldi, M., Borgani, S., & Dolag, K. 2007, *MNRAS*, 377, 2
- Navarro, J. F., Frenk, C. S., & White, S. D. M. 1996, *ApJ*, 462, 563
- Oemler, A. 1973, *ApJ*, 180, 11
- Pierini, D., Zibetti, S., Braglia, F., Böhringer, H., Finoguenov, A., Lynam, P. D., & Zhang, Y.-Y. 2008, *A&A*, 483, 727
- Puchwein, E., Springel, V., Sijacki, D., & Dolag, K. 2010, *MNRAS*, 406, 936
- Purcell, C. W., Bullock, J. S., & Zentner, A. R. 2007, *ApJ*, 666, 20
- Rudick, C. S., Mihos, J. C., Frey, L. H., & McBride, C. K. 2009, *ApJ*, 699, 1518 (R09)
- Rudick, C. S., Mihos, J. C., Harding, P., Feldmeier, J. J., Janowiecki, S., & Morrison, H. L. 2010, *ApJ*, 720, 569
- Rudick, C. S., Mihos, J. C., & McBride, C. 2006, *ApJ*, 648, 936 (R06)
- Seigar, M. S., Graham, A. W., & Jerjen, H. 2007, *MNRAS*, 378, 1575
- Sommer-Larsen, J., Romeo, A. D., & Portinari, L. 2005, *MNRAS*, 357, 478
- Springel, V., Yoshida, N., & White, S. D. M. 2001, *Nature*, 6, 79
- Springel, V. 2005, *MNRAS*, 364, 1105
- Trentham, N., & Mobasher, B. 1998, *MNRAS*, 293, 53
- Uson, J. M., Boughn, S. P., & Kuhn, J. R. 1991, *ApJ*, 369, 46
- Vilchez-Gomez, R., Pello, R., & Sanahuja, B. 1994, *A&A*, 283, 37
- Williams, B. F., et al. 2007, *ApJ*, 656, 756
- Willman, B., Governato, F., Wadsley, J., & Quinn, T. 2004, *MNRAS*, 355, 159
- Wu, Y.-T., & Jiang, I.-G. 2009, *MNRAS*, 399, 628
- Yang, X., Mo, H. J., & van den Bosch, F. C. 2009, *ApJ*, 693, 830
- Zibetti, S. 2008, *IAU Symposium*, 244, 176
- Zibetti, S., White, S. D. M., Schneider, D. P., & Brinkmann, J. 2005, *MNRAS*, 358, 949
- Zwicky, F. 1951, *PASP*, 63, 61

#### APPENDIX

##### BINDING ENERGY ALGORITHM

As described in Section 3.1, our algorithm to calculate the binding energy of luminous particles to the cluster galaxies works by measuring a spherical mass density profile for each galaxy, and analytically calculating the galaxy's potential as a function of

radius using Equation 1. In addition to the mass density profile itself, Equation 1 also requires that we find the truncation radius of the galaxy,  $r_{trunc}$ , or the radius beyond which there is no more mass contributing to the galaxy’s gravitational potential. Our procedures for calculating these quantities are described in detail below.

### Mass Density Profiles

The first step in determining the galaxies’ mass profiles is to identify individual galaxies, and measure their precise central positions and velocities. Fortunately, identifying galaxy cores is relatively straightforward, as they are defined by dense agglomerations of stellar particles. We simply use a friends-of-friends clustering algorithm with a linking length of 500 pc to find dense groups of stellar particles and use their mean positions and velocities as those of the galaxies. The positions and velocities of these galactic cores are insensitive to the choice of linking length, over a wide range of reasonably small values.

Around each galaxy core, we need to create a spherical mass density profile as a function of radius. Doing so, however, is complicated by two main factors. First, galaxy halos may not be intrinsically spherical, and we must therefore “average” over this non-sphericity. Additionally, the mass profiles of neighboring galaxies may overlap one another, whereas we wish to measure the mass profiles of galaxies individually. We address these two issues simultaneously by measuring a galaxy’s mass density profile independently in eight octants around the galaxy, in logarithmically spaced radial bins. We see the non-sphericity of the halo in the scatter of the density values between different octants. We find that this density scatter is approximated by a log-normal distribution, and thus take the density in a given radial bin to be the mean of the logarithm of the density values in each octant. Meanwhile, neighboring galaxies are easily identified as sharp peaks in the density profiles, which usually are present in only one or two octants. We can therefore minimize the impact of such galaxies by excluding the two highest density values at every radius. For isolated halos which do not have neighbors, we find that restricting our density profile to the six least dense octants does not significantly alter the galaxy’s density profile or gravitational potential.

The final step in creating the mass density profile of each galaxy is to smooth the profile. Smoothing is necessary in order to reduce two primary effects: 1) shot noise caused by the discreteness of the particles used to measure the density (because of our multi-resolution simulation approach, the outskirts of many galaxies are sampled by only a small number of relatively high-mass particles), and 2) short-lived variations in the mass distribution of the galaxies which may affect the density distribution at a particular time, but do not have an impact on the long-term binding state of stellar particles. Therefore, in order to effectively identify features in the density profiles, they are smoothed using a simple boxcar smoothing kernel. Additionally, because the analyses below rely on identifying features in a galaxy’s  $d\log(\rho)/d\log(r)$  profile, we then smooth this derivative profile, and recreate the final density profile from the central density and the smoothed derivative to ensure consistency. Again, testing has shown that the minor adjustments to the density profile created by this smoothing process have very little effect on the final binding energy profiles of the galaxies. Several example galaxy profiles are shown in Figure 9. The top plots of the figure show the galaxies’ density profiles, with the small points showing the raw density measurements in the eight octants, while the solid line shows the final smoothed profile. The smoothed  $d\log(\rho)/d\log(r)$  profiles are shown in the middle plots.

### Truncation Radius

A galaxy’s truncation radius,  $r_{trunc}$ , is essentially the “edge” of each galaxy, or the radius beyond which there is no mass which contributes to the galaxy’s gravitational potential. For the majority of galaxies within a cluster halo which do not reside at the center of the cluster, known as satellite galaxies, we essentially want to find the radius at which the background density of the cluster itself begins to dominate the galaxies’ mass distribution.

We illustrate the main features of our approach with the highly idealized example seen in Figure 10. Figure 10 shows two galaxy mass density profiles, a pure NFW profile — an isolated galaxy — and the same NFW halo embedded within a constant density background — a galaxy residing within a massive cluster potential. In the inner regions, the two halos are essentially identical. However, whereas the pure NFW halo continues to drop in density even at the largest radii, the embedded halo levels off at the background density. The different behavior of these two profiles can be very clearly seen in the plots of their derivatives,  $d\log(\rho)/d\log(r)$ , also shown in Figure 10. Whereas the slope of the pure NFW halo decreases from  $-1$  in the inner regions to  $-3$  at the largest radii, the embedded halo’s slope reaches a minimum and then increases to an asymptotic value of 0. This derivative curve clearly indicates that as the radius increases, the constant background density begins to dominate over the profile of the galaxy itself, and we can use the features of this curve to define the truncation radius. We have chosen to define the truncation radius as the point where the  $d\log(\rho)/d\log(r)$  slope exceeds  $-1$ , which is marked with a dotted line in Figure 10. From Figure 10, it is clear that qualitatively this is the radius at which the density profile is leveling out to the background density. Importantly, while this analysis clearly demonstrates the utility of our method for NFW galaxy halos, it is not dependent on the specific properties of the NFW profile, and is equally effective on any similar declining galaxy mass density profile.

The middle panels of Figure 9 show the  $d\log(\rho)/d\log(r)$  curves for our example simulation galaxies. The galaxies in Figure 9 show the same qualitative behavior as our idealized example in Figure 10, where the slope of the density profile decreases in the inner regions, and then reaches a minimum before increasing to  $d\log(\rho)/d\log(r) \approx 0$  at large radii. Extensive testing has shown that defining the truncation radius to be the point where the derivative is  $\geq -1$  is a robust measurement for the vast majority of simulation galaxies. The examples in Figure 9 demonstrate that this metric delineates the qualitative transition where the mass density profiles of the galaxies begin to level off and be dominated by the background cluster density. For galaxies of the same stellar mass, those which are at larger cluster-centric radii will generally have larger truncation radii than galaxies near the cluster center, due to the fact that the cluster’s background density decreases with radius. We illustrate this point with two disk galaxies of similar mass from cluster C2, but at two different cluster-centric radii. While each galaxy has a stellar mass of  $\approx 3 \times 10^{10} M_{\odot}$  and a half-light radius of  $\approx 3$  kpc, the galaxy which lies 850 kpc from the cluster center has a truncation radius of 140 kpc, while the galaxy at cluster-centric radius of 264 kpc has a truncation radius of only 40 kpc. The bottom plots in Figure 9 show the

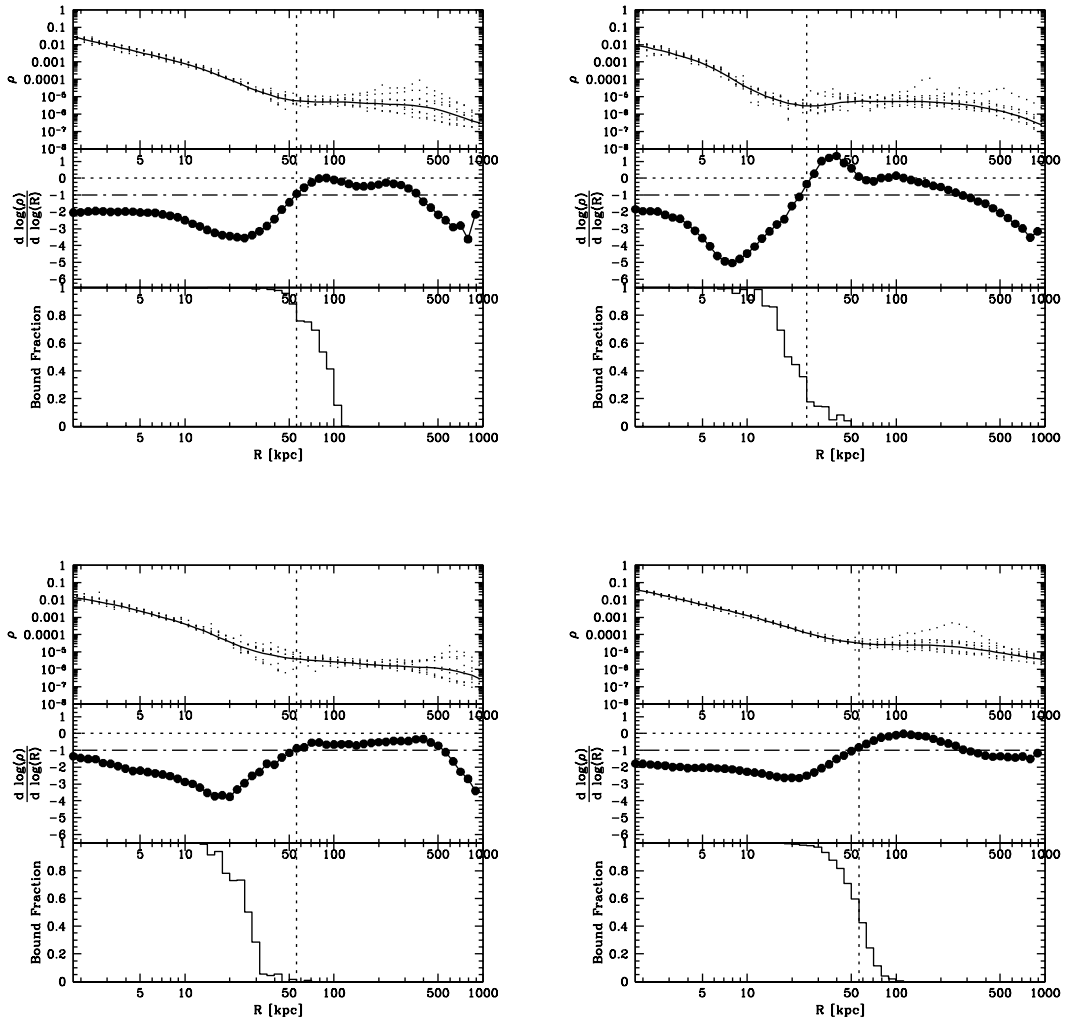


FIG. 9.— The density profiles of four typical satellite galaxies, each from a different cluster at  $z = 0$ . *Top*: Dots show the raw densities in each of the eight octants around the galaxy, while the solid line shows the final smoothed density profile. *Middle*: The  $d \log(\rho)/d \log(r)$  final smoothed  $d \log(\rho)/d \log(r)$  profile of the galaxy. The dotted line marks  $d \log(\rho)/d \log(r) = 0$  while the dot-dash line marks  $d \log(\rho)/d \log(r) = -1$ . *Bottom*: The fraction of luminous particles at each radius which are bound to the galaxy. The vertical dotted line running through all three plots shows the truncation radius of the galaxy.

fraction of the stellar particles bound to each galaxy as a function of radius. Each galaxy shows a similar pattern, where almost all the stellar mass at small radii is bound, and there is a fairly sharp transition at or near truncation radius where the vast majority of stellar mass becomes unbound.

There is one particularly important instance, however, when the assumptions used in the algorithm described above break down. For galaxies which sit very near the center of the cluster, especially cD galaxies, the paradigm of a galactic halo embedded within a locally constant density background does not apply. Instead, the mass density profiles of these galaxies are essentially indistinguishable from those of the cluster as a whole. Figure 11 shows the density profiles of two central galaxies, from clusters C2 and B35 at  $z = 0$ . As expected, these density profiles look like cluster-mass NFW profiles and show no indication of leveling off at radii up to 1 Mpc. Fundamentally, these galaxies do not have dark halos which are independent of the overall cluster potentials, and thus any mass bound to the cluster is then bound to the central galaxies. This, of course, would completely obviate our definition of ICL, in which ICL is luminous particles bound to the cluster but no galaxy within the cluster, since *all* luminous particles would be bound to the central galaxy.

Thus, in defining  $r_{trunc}$ , central galaxies must be treated as a special case. This issue is compounded by the fact that while central galaxies in massive clusters are readily identified by eye, there are other scenarios in which the same conditions hold. For instance, galaxies at the center of group-mass halos will also be indistinguishable from the overall group mass distribution. This makes it extremely difficult to implement such a binding energy measurement technique at higher redshifts, when the cluster mass is contained in a number of smaller groups which later merge to form the  $z = 0$  cluster. In order to efficiently automate the calculations, we have simply imposed a maximum truncation radius (described below), and thus it is not necessary to manually

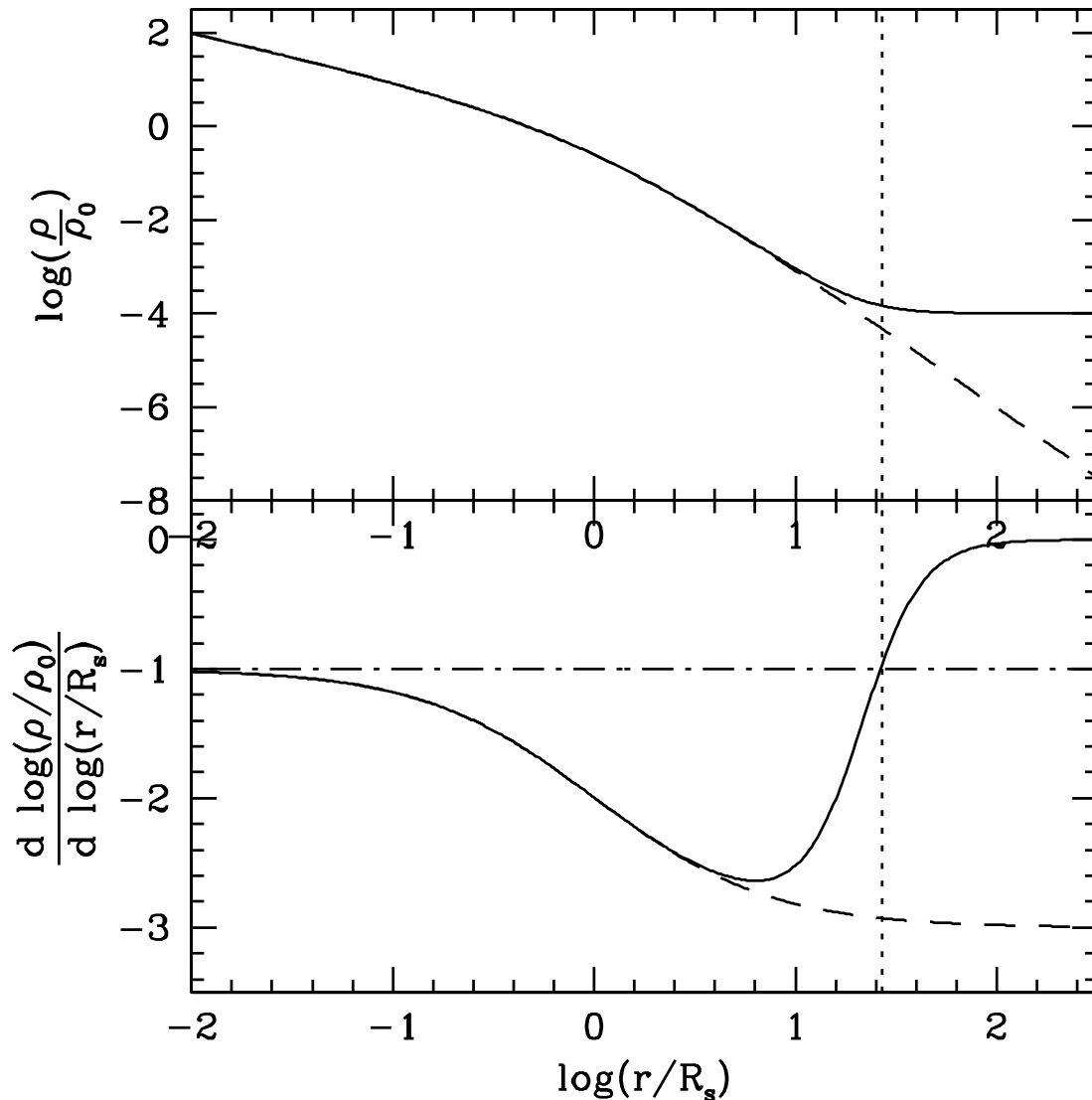


FIG. 10.— An idealized NFW profile, with unit scale radius,  $R_s$ , and characteristic density,  $\rho_0$ . *Dashed Lines*: Pure NFW profile, indicative of an isolated galaxy. *Solid Lines*: NFW profile embedded in a constant density background, indicative of a galaxy within the cluster environment. *Top*: The galaxies' density profiles. *Bottom*: The galaxies'  $d\log(\rho)/d\log(r)$  profiles. The dotted vertical line indicates the truncation radius while the dot-dash line marks  $d\log(\rho)/d\log(r)=-1$ .

specify any central galaxies.

#### *Binding Energy Free Parameters*

Given the algorithm described above, the major free parameter which can be varied is the maximum truncation radius. This parameter primarily affects the binding state of particles due to the change in potential of the clusters' central galaxies. Our preferred value for the maximum truncation radius is 100 kpc. While several of the largest satellite galaxies have truncation radii based on their density profiles which are slightly larger than this limit, up to  $\approx 200$  kpc, this has very little effect on the total measured ICL in the cluster. We illustrate this effect with a series of tests on cluster C2, where we calculate the luminosity bound to the satellite galaxies (i.e., all galaxies except for the central galaxy) When the maximum truncation radius is set to 100 kpc, 42.3% of the luminosity is bound to the satellite galaxies, while when the maximum truncation radius is 200 kpc 44.9% of the cluster luminosity is bound to these galaxies. Moreover, changing the algorithm so that  $r_{trunc}$  is defined as the point where the  $d\log(\rho)/d\log(r)$  curve reaches a minimum ( $d^2\log(\rho)/d\log(r)^2=0$ ), has a similarly small effect on the satellite galaxies. This analysis demonstrates that the gravitational potentials of satellite galaxies are fairly readily defined, and there is a relatively small amount of material that is only marginally bound/unbound from these galaxies.

The cluster ICL fraction, is, however, very sensitive to the truncation radius of the *central* galaxy. Whereas the maximum truncation radius only marginally affects a small number of satellite galaxies, this maximum radius will always be the truncation radius of the central galaxy, and has a very large effect on its gravitational binding energy. We again demonstrate with tests on cluster C2, this time running the binding energy algorithm on all galaxies, including the central galaxy. With a truncation radius

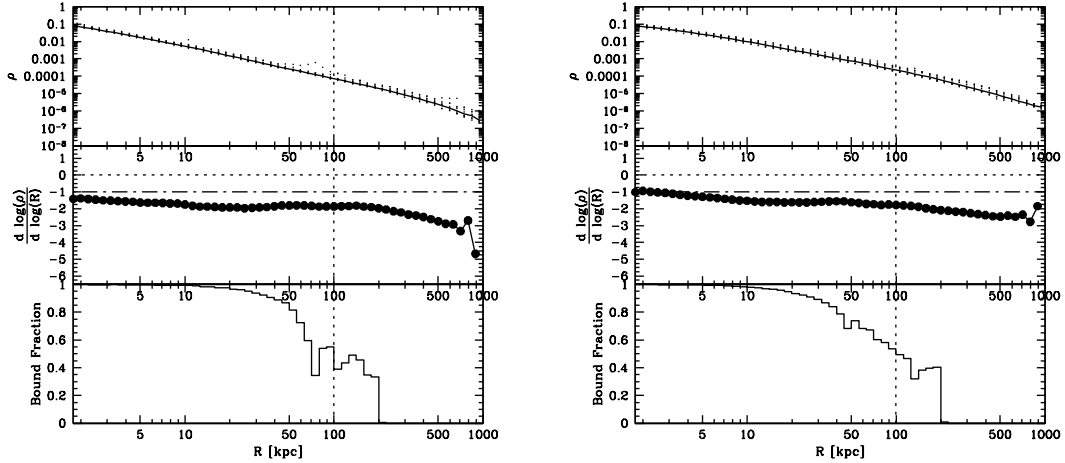


FIG. 11.— The density profiles of the massive central galaxies from clusters C2 (left) and B35 (right) at  $z = 0$ . Plots are the same as in Figure 9.

of 100 kpc, 20.0% of the cluster luminosity is unbound to any galaxy, whereas only 9.5% of the cluster luminosity is unbound when  $r_{trunc}$  is set to 200 kpc. From the previous tests, we know that the vast majority of this change comes from the central galaxy. From Figure 11, it is clear that the mass density of the central galaxy in this radial range is very high, and thus small changes in the mass density or luminosity profiles of the galaxy to use in defining the truncation radius, any value will be somewhat subjective and arbitrary. Moreover, because the cluster’s luminosity is so centrally concentrated (see Section 4), the binding energy of the central galaxy has a huge effect on the total ICL fraction of the cluster.

The bottom plots of Figure 11 show the fraction of the clusters’ luminous mass bound to the central galaxies as a function of radius, similar to Figure 9. These galaxies do not show nearly as sharp a transition from bound to unbound near the truncation radius. Furthermore, a substantial fraction of the clusters’ luminosity is bound to the central galaxies, even at very large radii. We have therefore limited the binding energy calculations such that stellar particles beyond twice the truncation radius cannot be bound. This restriction has almost no effect on the satellite galaxies, but for cluster C2 the ICL fraction increases by  $\approx 4\%$  due to particles no longer being bound to the central galaxy.